Nanoscale Active Sites for the Hydrogen Evolution Reaction on Low Carbon Steel

L. C. Yule,[a,b] *V. Shkirskiy*,[a] *J. Aarons*,[c] *G. West*,[b] *C. L. Bentley*,[a*] *B. A. Shollock*[b,d,*] *and P. R. Unwin*[a,*]

[a]Department of Chemistry, [b]Warwick Manufacturing Group and [c]Department of Physics University of Warwick, Coventry CV4 7AL, U.K.

[d]Kings College London, Strand, London, WC2R 2LS

*Corresponding Authors: c.bentley.1@warwick.ac.uk (C.L.B.); barbara.shollock@kcl.ac.uk (B.A.S.); p.r.unwin@warwick.ac.uk (P.R.U.)

Abstract. To fully elucidate the structural controls on corrosion-related processes at metal surfaces, experimental measurements should correlate and compare directly structure and activity at the scale of surface heterogeneities (*e.g.*, individual grains, grain boundaries, inclusions *etc.*). For example, the hydrogen evolution reaction (HER), which usually serves as the cathodic counterpart to anodic metal dissolution in acidic media, may be highly sensitive to surface microstructure, highlighting the need for nanoscale-resolution electrochemical techniques. In this study, we employ scanning electrochemical cell microscopy (SECCM) in conjunction with co-located scanning electron microscopy, electron backscatter diffraction, and energy dispersive X-ray spectroscopy to elucidate the relationship between surface structure/composition and HER activity on low carbon steel in aqueous sulfuric acid (pH ≈ 2.3). Through this *correlative electrochemical multimicroscopy* approach, we show that the HER activity of the low index grains (slightly) decreases in the order (100) > (111) > (101), with grain-dependent free energy of hydrogen adsorption (calculated for the low index planes of iron using density functional theory, DFT) proposed as a tentative explanation for this subtle structural-dependence. More significantly, we show that the HER is greatly facilitated by sub-micron surface defects, specifically grain boundaries and MnS inclusions, directly identifying these heterogeneities as potential "cathodic sites" during (atmospheric) corrosion. This study demonstrates the considerable attributes of correlative SECCM for identifying nanoscale active sites on surfaces, greatly aiding understanding of corrosion and electrocatalytic processes.

Introduction

Resolving the relationship between surface microstructure (*e.g.*, crystallographic orientation, inclusions and grain boundaries) and electrochemical processes at metals and alloys is vital to advance understanding of corrosion. Although the structural and compositional heterogeneities of metal surfaces are routinely studied using *ex situ* high-resolution microscopy/spectroscopy,[1] corrosion measurements are often performed with classical macroscopic or "bulk" electrochemical techniques[2] that are unsuitable for assessing heterogeneously active surfaces.[3]

Scanning electrochemical cell microscopy (SECCM) provides a means of making nanoscale electrochemical measurements at distinct target sites by using the droplet (meniscus) formed at the end of an electrolyte-filled nanopipet to wet a small area of an electrode surface and create a local electrochemical cell.[4-6] SECCM is the next-generation of the well-known electrochemical droplet cell (EDC) technique,[7] and differs from the more widely-used scanning electrochemical microscopy (SECM)[8-9] in that with SECCM only small portions of a surface are exposed to solution, through brief meniscus contact from a nanopipet probe at a series of pixels, and electrochemical properties are measured *directly* (*e.g.*, by voltammetry, chronoamperometry, etc.) at each point. This attribute is particularly beneficial for highly reactive surfaces that undergo corrosion. In further contrast to SECM, the SECCM response also reveals the corresponding surface topography synchronously, with ≈2 nm vertical resolution having been demonstrated,[10] so that the surface location of nanoscale electrochemical measurements are easily identified. Recently, SECCM has been employed to make local

electrochemical measurements on single nanoparticles,[10-12] transition metal dichalcogenides,[13-14] polycrystalline metals[15-17] and sp^2 carbon materials[18] using nanopipets with diameters as small as ≈30 nm.[10-11]

SECCM is a potentially powerful tool for corrosion-related research, as demonstrated by proof-of-concept studies that revealed the role of microstructure on the electrochemical (corrosion-related) behavior of low carbon steel in neutral pH solutions.[4] SECCM greatly advances the capabilities of conventional EDC techniques by improving spatiotemporal resolution, throughput (number of measurements on a sample), and the density of data, among other key features.[19] In the present study, we focus on the influence of surface microstructure on the rate of the hydrogen evolution reaction (HER) on low carbon steel in aqueous sulfuric acid (pH ≈ 2.3). Although the HER has traditionally been explored in the context of electrocatalysis,[20] this process serves as the cathodic counterpart to anodic metal dissolution during corrosion in acidic media.[21] In addition to the SECCM "droplet-cell" configuration mimicking the conditions of atmospheric corrosion,[3] low carbon steel is frequently exposed to acid media in many industrial applications, including acid pickling and acid cleaning/descaling.[22] Thus, elucidating the structural-dependency is critical to understanding and further predicting the characteristics of galvanic corrosion cells that are formed on macroscopic metal surfaces during practical use.

In the present study, SECCM has been employed in conjunction with the co-located microscopy techniques scanning electron microscopy (SEM), electron backscatter diffraction (EBSD) and energy-dispersive X-ray spectroscopy (EDS) to explore the role of crystallographic orientation, grain boundaries and MnS inclusions on the rate of HER at low carbon steel. The study significantly advances our previous work,[4] with considerable improvements in spatial-resolution and imaging time, in addition to the implementation of density functional theory (DFT) calculations to support the grain-dependent electrochemical data. Sub-microscale surface defects (*e.g.*, grain boundaries and MnS inclusions) are revealed as important cathodic sites.

Experimental Section

Electrode material and chemical reagents. The low carbon steel sample used in this study (composition detailed in Table 1) was of size 5 × 21 × (thickness) 2 mm and was mounted in a carbon-based mounting compound (KonductoMet. Buehler, U.S.A) using a Buehler SimpliMet 4000 Mounting Press (Buehler, U.S.A). Once mounted, the sample was polished on a polishing cloth (TriDent. Buehler, U.S.A) using 9 µm, 3 µm and 1 µm polishing suspensions (MetaDi Supreme Suspension. Buehler, U.S.A). To finish, the sample was polished with 0.05 µm alumina suspension (MasterPrep Alumina. Buehler, U.S.A). The sample was subsequently washed with acetone, soapy water and deionized water, before being blown dry. Sulfuric acid (H_2SO_4, Merck, 96%) was used as supplied and diluted using ultra-pure deionized water (Integra HP, Purite, U.K.), which has a resistivity of 18.2 MΩ cm at 25°C.

Table 1. Chemical composition of the low carbon steel, determined using energy dispersive X-ray spectroscopy.

%	C	Mn	Si	Cr	Al	P	S	Cu
Low Carbon Steel	0.05	0.3	<0.03	0.06	0.03	<0.02	<0.02	0.04

Surface characterization. SEM, EBSD and EDS characterization was performed with a Zeiss SUPRA FE-SEM (Zeiss, Germany), using a Nordlys EBSD detector (Oxford Instrument, U.K.) and an X-max 50 mm^2 energy-dispersive X-ray spectroscopy (EDS) detector (Oxford Instrument, U.K.). SEM images and EDS data were collected at 10 keV, whereas EBSD images were collected at 20 keV, with the sample tilted at 70° to the detector. Following EBSD characterization, grains selected for further

analysis were either on or close to the low index orientations, (100), (101) and (111). The criterion set in this study was <10º deviation from the desired orientation.

SECCM probe fabrication. Borosilicate capillaries (GC120F-10. Harvard Apparatus, U.S.A) were pulled (P-2000 pipet puller, Sutter Instruments, U.S.A) to give 2 nanopipets with an end-diameter of approximately 150 nm (as confirmed by SEM). Pulling parameters: Line 1: HEAT 350, FIL 3, VEL 30, DEL 220, PUL -; Line 2: HEAT 350, FIL 3, VEL 40, DEL 180, PUL 120. For use, each pipet was filled with 5 mM H_2SO_4 which formed a droplet (meniscus) cell at the pipet tip. A small amount of silicone oil (Fluka Analytical) was inserted on top of the sulfuric acid solution (from the back) in order to reduce the evaporation from the pipet, as previously reported.[4, 13] A Pd/H_2 quasi reference counter electrode (QRCE) was then inserted into the electrolyte. The Pd/H_2 QRCEs were prepared by hydrogenating Pd wire, of thickness 0.125mm (Goodfellow, U.K.), in 50 mM H_2SO_4. The reference potential was calibrated to the Ag/AgCl (3.4 M KCl, eDAQ, Australia) scale, after measurements, by monitoring the "open circuit potential" of the QRCE over a period of 30 minutes.

SECCM configuration. The SECCM set up[4, 11] is shown schematically in Figure 1a. In brief, during a typical SECCM experiment, the nanopipet probe was mounted on a z-piezoelectric positioner (P-753.2 LISA. PhysikInstrumente, Germany) and the substrate of interest (low carbon steel, herein) was mounted on a *xy*-piezoelectric positioner (P-621.2 PIHera, PhysikInstrumente). The probe was positioned close to the surface of the low carbon steel substrate using micropositioners (M-461,

Newport, U.S.A.), aided by visualization with a PL-B776U camera equipped with a 4× lens (Pixelink, U.S.A.). Micropositioners and piezoelectric positioners were used for coarse and fine control of the probe/substrate in *xyz* space, respectively. During the automated approach (5 μm/s, herein), a voltage (0.463 V vs Ag/AgCl) was applied to the QRCE within the probe such that a surface current (i_{surf}) would flow upon droplet contact with the substrate (*i.e.*, the electrochemical circuit was closed). An i_{surf} threshold of *ca.* 2 pA was used to detect when meniscus contact with the substrate had been made, immediately halting the *z*-approach (*e.g.*, see the Supporting Information, Figure S1). Note that the pipet itself did not make physical contact with the substrate.

Upon meniscus contact with the substrate, chronoamperometric ($i-t$) measurements were made at a series of predefined locations (*i.e.*, in a grid) to build up an 'electrochemical map' of the surface. The probe was retracted from the surface after each measurement before being moved to the next location in a chronoamperometric 'hopping mode'. A visible droplet 'footprint' was left on the surface after each $i-t$ experiment, which was visible in FE-SEM and used for subsequent co-located (*ex situ*) surface analysis with EBSD and/or EDS. Measurements of the droplet 'footprint' sizes are displayed in the Supporting Information, Figure S2.

The entire SECCM apparatus was on mounted on an optical table (RS2000. Newport, U.S.A) which was supported by vibration isolating supports (S-2000, Newport, U.S.A) and shielded with a Faraday cage equipped with heat sinks and vacuum panels to minimize noise and variations in

temperature. The QRCE potential was controlled with respect to ground and the current flowing at the substrate (at ground) was measured using a home-built electrometer. Current was recorded as an average of 129 samples taken every 4 μs (*i.e.*, approximately every 0.5 ms). A home-built 8th order (low-pass) brick-wall filter unit (time constant = 1 ms) was utilized during data (current) collection. Data acquisition and fine control of all instrumentation was achieved using an FPGA card (PCIe-7852R) controlled by a LabVIEW 2016 (National Instruments, U.S.A) interface running the publically-available Warwick Electrochemical Scanning Probe Microscopy (WEC-SPM, www.warwick.ac.uk/electrochemistry) software. The experimental data were processed using the Matlab R2016b (Mathworks, U.S.A) and OriginPro 2016 64bit (OriginLab, U.S.A) software packages.

Density functional theory calculations. We performed plane wave basis set Kohn-Sham Density Functional Theory (DFT)[23] calculations with a plane-wave kinetic energy cut-off of 600 eV, which was found to give converged binding energies to 2 significant figures. Calculated data were also converged with respect to Brillouin zone sampling, using a Monkhurst-Pack grid of 9 × 9 × 1 k-points with no origin shift.[24] To account for the core atomic states, ultrasoft pseudopotentials[25] from the pslibrary[26] suite were used in Quantum Espresso[27] for all calculations of hydrogen adsorption. Surfaces were represented as a slab model of iron, with a thickness of 7 layers. In the *z*-direction, perpendicular to the slab, a vacuum gap of 7.5 Angstroms was employed to simulate open boundary conditions. Due of the propensity of hydrogen to introduce a long-range electric dipole moment, we corrected for spurious

interactions through the *z*-boundary by using the self-consistent Neugebauer-Scheffler dipole correction scheme.[28]

The methodology for finding the ground state configuration of the cells (bare metal surface energy) was first to perform a variable-cell geometry optimization of the bulk metal cell to find a converged lattice parameter, which we found to be 2.759 Å. We then formed vacuum slabs of the bulk lattice parameter and allowed the surface layers to relax in a fixed-cell geometry optimization, while constraining the position of the two layers furthest from the simulated surface. To perform adsorption studies, hydrogen atoms were added onto the bare metal surface configuration in positions close to the high symmetry adsorption sites (see Supporting Information, Fig. S6), with a perpendicular separation of approximately 2 Å. These configurations were allowed to relax, while keeping the deepest two metal layers constrained, yielding the minimized energies of metal cell and hydrogen in each adsorption configuration. To compute binding energies, E_{ads}, we used the equation:

$$E_{\mathrm{ads}} = E_{\mathrm{H+bare}} - E_{\mathrm{bare}} - E_{\mathrm{H}} \quad (5)$$

where $E_{\mathrm{H+bare}}$, E_{bare}, and E_{H} refer to the energy of the plane with a hydrogen atom adsorbed onto it, the energy of the bare plane and the energy of a hydrogen atom in the center of a vacuum box, respectively. The same parameters were used for the slab calculations.

Throughout these calculations we used an electronic energy convergence tolerance of 2×10^{-6} eV. The Gaussian electronic smearing scheme was used, with a smearing width of 0.1 eV, to account

for the metallic nature of this system and the electronic structure was optimized using the Pulay DIIS scheme.[29] We used the BFGS geometry optimization scheme[30] with tolerances of 2×10^{-5} eV/atom in energy, 0.05 eV/Å in maximum force, 0.002 Å in maximum atomic displacement and, in the case of the variable-cell bulk geometry optimization, 0.1 GPa maximum stress.

Results and Discussion

SECCM: operational principles. In this study, we employ the single barrel SECCM protocol, detailed in Figure 1a, with a pixel acquisition rate of ≈1 s pixel^{-1} using a probe diameter of 150 nm. A potential, $-E_{app}$, was applied to a Pd/H_2 quasi reference counter electrode (QRCE) inserted into the electrolyte in an SECCM nanopipet probe, with respect to the substrate (working electrode) surface. Note that all potentials herein have been calibrated to the Ag/AgCl (3.4 M KCl) scale, after measurements. The SECCM probe was approached to the substrate at a series of predefined locations, and when meniscus contact was made (without physical contact from the nanopipet), a current, i_{surf}, flowed as the electrochemical circuit was closed (*e.g.*, Supporting Information, Figure S1). This was used as the feedback signal to halt the approach of the probe (and map the surface topography from the corresponding *x*,*y*,*z* coordinates). Upon surface-meniscus contact, electrochemical measurements (Figure 1b) were carried out within the confines of the wetted area, the 'footprint' of which was visualized, after experiments, using SEM, with example data shown in Figure 1c.

Herein, chronoamperometric (current-time, $i-t$) measurements were made, by stepping E_{app} at each scanning point. The pulse potential was selected after inspection of the linear-sweep voltammogram obtained from low carbon steel in 5 mM H_2SO_4 using the SECCM configuration, with typical data shown in the Supporting Information, Figure S2. During the approach, E_{app} was in the passive region (0.463 V vs Ag/AgCl), which provided a reliable feedback signal for positional control

(see Figure S1). Upon meniscus contact of the probe with the surface, the potential was maintained at the approach potential for a further 10 ms which 'preconditioned' the surface by forming a thin passive film. E_{app} was then stepped to a driving cathodic potential (-1.337 V vs Ag/AgCl) to quickly reduce the passive film and produce a stable substrate surface current, predominantly from the hydrogen evolution reaction (HER):

$$2H^+ + 2e^- \rightarrow H_2 \quad (1)$$

Note that the oxygen reduction reaction (ORR) only makes a minor contribution to i_{surf} at $E_{app} = -1.337$ V vs Ag/AgCl, confirmed by comparing cyclic voltammograms obtained in the presence and absence of air (Supporting Information, Figure S2). The current-time transient during the preconditioning is at the background level due to the comparatively low magnitude of the currents relative to the reduction pulse, however, it can be viewed in isolation in the Supporting Information, Figure S3. This protocol was preferable to running a full voltammetric (current-potential, $i-E$) curve in the present study for three main reasons. The first reason was to minimize the scanning time (≈1 s pixel^{-1}, compared to ~85 s pixel^{-1} previously).[4] The second reason was that biased steel surfaces promote potential-dependent electrowetting[31] and a potential sweep approach may have introduced uncertainty as to the wetted area, whereas with a fixed potential we were able to measure the wetted area with confidence, after experiments (*vide infra*). The third reason is that sweeping the potential through the active dissolution region (*i.e.*, the large anodic peak seen in Figure S2) causes significant damage to the surface and loads

the near-surface electrolyte region (*i.e.*, the meniscus cell) with soluble Fe-species, which can electro-deposit in the potential-region where the HER occurs, complicating the analysis.

To confirm that any pre-existing passive film was fully reduced upon approaching the steady-state current for the HER (achieved on the 10 ms timescale, *vide infra*), the total charge passed during the reduction pulse was compared to the approximate charge required to remove a film of Fe_2O_3, within the confined area of the droplet cell. Taking 5 nm as a conservative estimate of the thickness of the passive film on low carbon steel (in reality, likely to be <5 nm thick, as previously reported[32]), the charge required to remove the film is <20% of the charge passed during the decaying portion of the reduction pulse, detailed in the Supporting Information, Figure S4. Therefore, it is certain that surface currents arising at the end of the reduction pulse (*i.e.*, beyond 7 ms, *vide infra*) arise predominantly from the HER. The cathodic potential applied is also −0.85 V beyond where the passive potential range ends (from examination of Figure S2), therefore there is a considerable driving force for any passive film to be removed.

The hopping distance (separation between neighboring pixels) was set conservatively to 800 nm in order to avoid overlap between points of the scan (*i.e.*, to ensure that each measurement was independent of the last; Figure 1c). This distance was much larger than the tip diameter (≈150 nm) due to wetting of the metal surface, consistent with previous reports of the enhanced wetting of micro-droplets on steel during cathodic polarization.[31] After identifying the scanned area with SEM, co-located

EBSD was performed (*e.g.*, Figure 1d), so that electrochemical activity could be correlated directly with the underlying grain structure (*vide infra*). Furthermore, the wetted area could be measured to calculate local current densities. The wetted area *was ca.* 400 nm diameter on all grains, with no grain dependence, as shown in the Supporting Information, Figure S5. For reference, 100 pA detected with the SECCM configuration, herein, corresponds to a current density of *ca.* 80 mA cm^{-2}. It should be noted that the individual grains were also identifiable from the *z*-height (topographical) data, collected synchronously with the spatially-resolved $i-t$ data during SECCM imaging (Figure 1e). The <20 nm height difference between the individual grains is due to surface-orientation-dependent polishing rates, and that surface height variation can be detected by SECCM highlights the excellent topographical imaging capability of the technique.

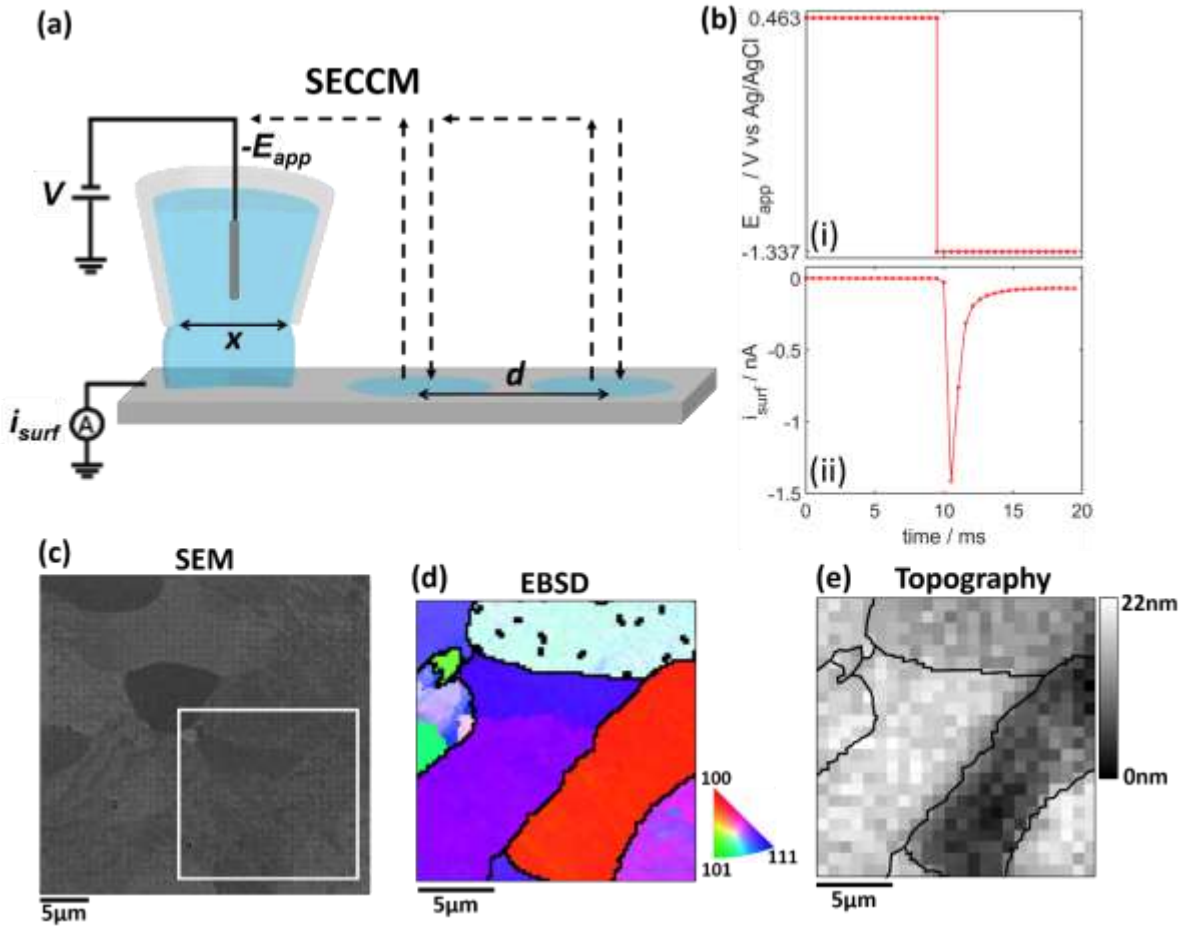

Figure 1. (a) Schematic showing the SECCM hopping-mode protocol used to make spatially resolved electrochemical (i_{surf}–t) measurements on the substrate (working electrode) surface. The arrows indicate the path taken by the probe during the scanning. For this investigation, the diameter of the probe, x, was 150 nm and the 'hopping distance', d, was 800 nm. The nanopipet was filled with 5 mM H_2SO_4 solution (pH ≈ 2.3) and equipped with a Pd/H_2 QRCE. **(b) (i)** Landing potential, E_{app} = 0.463 V vs Ag/AgCl for 10 ms followed by E_{app} = −1.337 V vs Ag/AgCl for 10 ms and **(ii)** representative i_{surf}–t transient, taken from a single hop of a scanning experiment. **(c)** SEM image of a (40 × 40) pixel^2 (32 × 32) µm^2 grid, after SECCM-scanning, with the array of dots 'footprints' denoting the locations of the electrochemical measurements. **(d)** EBSD map obtained from the area delineated by the white box in (c)**. (e)** Corresponding topographical image of the area in highlighted in (c) and (d), constructed from the synchronously obtained z-height data (piezo-position at meniscus contact) in SECCM (no interpolation of data).

Hydrogen evolution reaction: crystallographic dependence. In this section, we investigate the dependence of the HER rate (measured through the catalytic current) on the crystallographic orientation of low carbon steel, where the high spatial-resolution afforded by SECCM allows us to make a statistically significant number of measurements on individual grains presented by a low carbon steel sample in a 'pseudo single-crystal' approach.[33] The average i_{surf}–t response extracted from all scanning points after stepping the potential from 0.463 V to −1.337 V vs Ag/AgCl for 10 ms is shown in Figure 1b. During the first ~6 ms of the pulse, i_{surf}, arising from the HER, is not at steady-state and is also influenced from the finite rise time of the measurement (see Experimental Section for details). After ~6 ms, i_{surf} approaches a steady-state and as a result we focus on this section of the transient for analysis. Note that the relatively short time to steady-state is expected based on the high diffusion coefficient of the hydronium ion (H_3O^+) in aqueous media (9.3×10^{-5} cm^2 s^{-1}, measured previously[34]) combined with the quasi-radial diffusion conditions inherent to the SECCM droplet cell configuration, particularly with the fine probe (*ca.* 150 nm in diameter) employed herein, as discussed in depth previously.[35]

EBSD maps and corresponding spatially-resolved i_{surf} maps taken from two areas of the low carbon steel surface are shown in Figure 2a and b, respectively. Note that the i_{surf} maps displayed in Figure 2b (and beyond) are calculated by averaging i_{surf} in the 7.2 – 9.8 ms period (*i.e.*, last 6 data points) at the end of the i_{surf}–t transient, justified above. Comparing the EBSD maps to the corresponding spatially-resolved i_{surf} maps reveals a subtle correlation between the crystallographic orientation and the

HER activity of the low carbon steel surface. A time-resolved video of the map of i_{surf} values throughout the transient is shown in the Supporting Information, Movie S1.

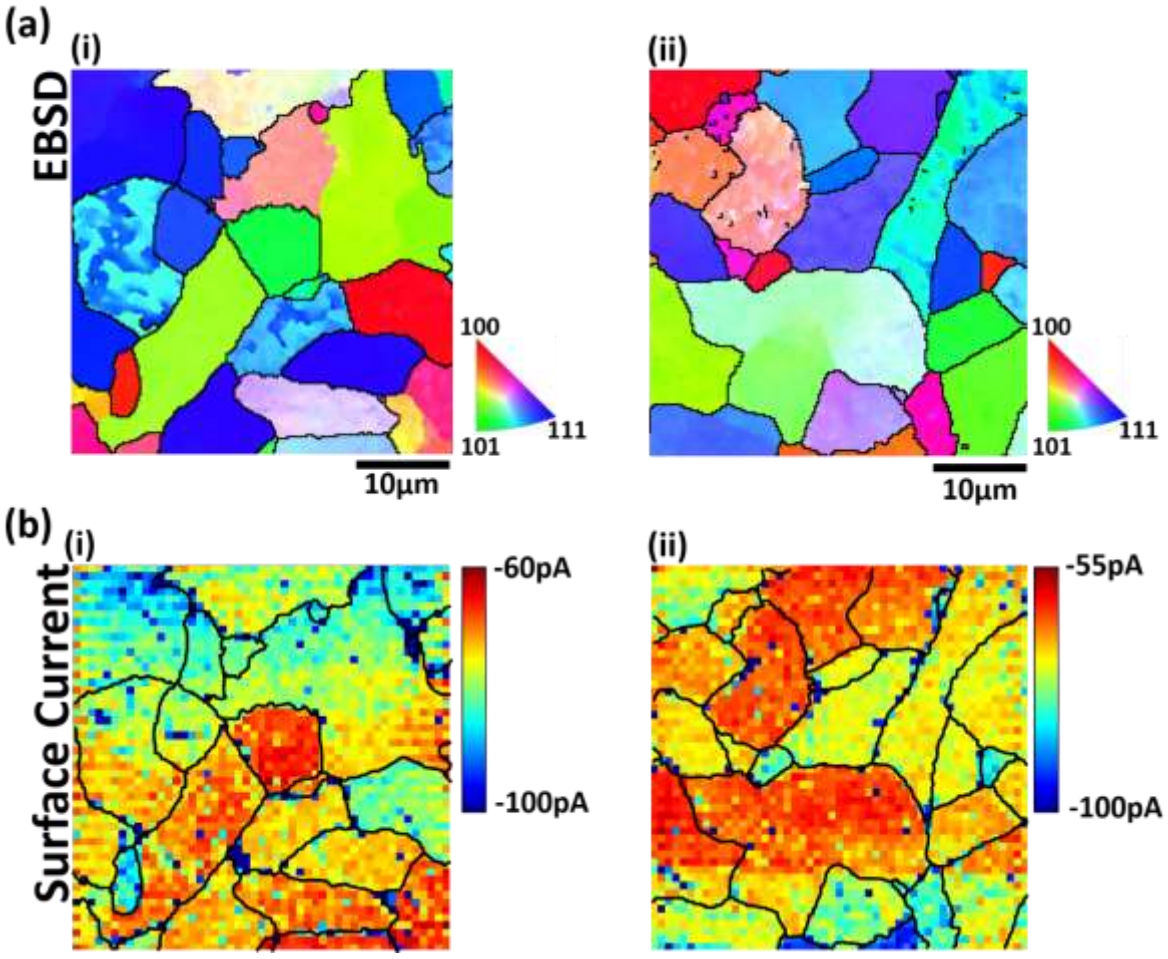

Figure 2. (a) EBSD maps of the areas of the low carbon steel surface that were characterized with SECCM. **(b)** Spatially-resolved i_{surf} maps (2500 pixels) over a (40 × 40) µm^2 area, corresponding to the areas shown above in **(a)**. The i_{surf} values are the average of the last six data points (*i.e.*, 7.2 to 9.8 ms) and the data are presented as the recorded currents (no interpolation). With the SECCM footprint areas defined in the text, the maximum and minimum currents of 100 pA and 55 pA corresponds to current densities of *ca.* 80 and 44 mA cm^{-2}, respectively. The maps were taken at E_{app} = −1.337 V vs Ag/AgCl with a probe of 150 nm diameter containing 5 mM H_2SO_4.

As alluded to above, the HER has been studied predominantly in the context of electrocatalysis, primarily on Pt-based materials,[36] for which the crystallographic orientation (structure) dependence is hotly debated.[37-38] Due to comparatively poor catalytic activity, Fe-based materials (*e.g.*, steel) have received significantly less attention, which is perhaps surprising considering the important role of cathodic processes such as the HER in the corrosion of steel. The majority of literature concerning hydrogen-related processes on steel focuses on hydrogen embrittlement, and the diffusion of hydrogen into bulk steel.[39]

In order to tentatively explain the grain-dependent HER rates on low carbon steel (*i.e.*, Figure 2), we performed DFT calculations, focusing on the low index planes, *i.e.*, (100), (101) and 111) of the body centered cubic (BCC) structure of iron. Given that the iron content of the substrate is ~99.5% (see Experimental Section), iron is considered to be representative of the low carbon steel surface and therefore appropriate for DFT. Figure 3a identifies the grains that possess an orientation within 10° of the (i) (100), (ii) (101) and (iii) (111) low index planes (shown schematically for a BCC unit cell). Presented in Figure 3b is a histogram showing the average surface currents measured between 7.2 to 9.8 ms for all $i-t$ measurements taken on the low index grains (identified in Figure 3a), which visually emphasizes why making multiple measurements on each grain improves the validity of any grain dependent trends. Evidently, the HER activity of the low index grains of the low carbon steel surface

decreases in the order (100) > (111) > (101), albeit only slightly (*vide infra*), with mean i_{surf} (between 7.2 and 9.8 ms) values of 80 ± 4, 71 ± 2 and 66 ± 3 (mean ± standard deviation), respectively.

Note that although the i_{surf} values between 7.2 and 9.8 ms can be taken as qualitative indicators of relative HER activity, due to the cathodic potential applied (−1.337 V vs Ag/AgCl, see Figure S2) and low bulk concentration of H^+ ($[H_2SO_4]$ = 5 mM), there is some contribution from mass transport (*i.e.*, the HER is not purely surface-kinetic controlled). To illustrate this, considering that the diffusional flux in SECCM is approximately 10% of that for the same sized disk electrode,[13, 40] and the diffusion coefficient of the hydronium ion (H_3O^+) is 9.3×10^{-5} cm^2 s^{-1} in aqueous media,[34] a steady-state limiting current (i_{ss}) of *ca.* −150 pA is expected from a probe of 150 nm diameter, assuming that mass-transport occurs solely by diffusion. (Note that under steady-state conditions the probe geometry, rather than wetted area determines the local mass-transport rate). As the average i_{surf} values from 7.2 to 9.8 ms (−66 to −80 pA) are *ca.* half of i_{ss}, E_{app} = −1.337 V vs Ag/AgCl lies near the voltammetric half-wave potential, where the reaction (*i.e.*, HER) is under mixed kinetic-diffusion control. Thus, the absolute mean i_{surf} values between 7.2 and 9.8 ms cannot be taken as quantitative measures of the relative HER kinetics (*i.e.*, the relative exchange currents, i_0), but do provide a qualitative indicator of the trends in activity, as discussed in further detail below.

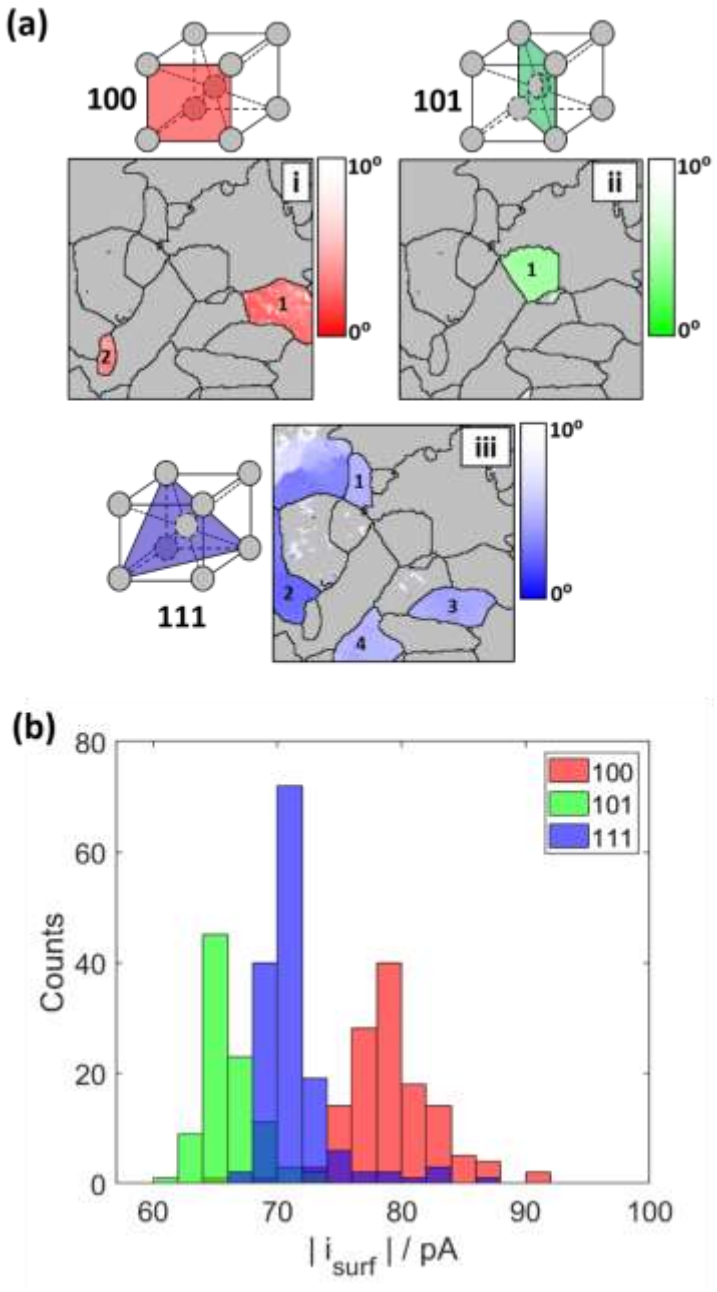

Figure 3. (a) Grains within the area scanned with SECCM that have a crystal orientation within 10° of the (i) (100) (ii) (101) and (iii) (111) low index orientations of low carbon steel. **(b)** Histogram of the average surface currents, i_{surf}, measured from 7.2 to 9.8 ms from each of the measurement landing on the low index grains indicated in (a).

To explore possible explanations for the grain-dependent HER activities, one must first consider the HER mechanism, which is generally accepted to follow one of two electrocatalytic pathways on metal surfaces in acidic media, Volmer-Heyrovsky or Volmer-Tafel:[20]

$$H^+ + e^- + * \rightarrow H^* \quad (2)$$

$$H^* + H^+ + e^- \rightarrow H_2 + * \quad (3)$$

$$2H^* \rightarrow H_2 + 2^* \quad (4)$$

where * donates an adsorption site on the metal surface, and Equations 2, 3 and 4 refer to the Volmer, Heyrovsky and Tafel step, respectively. The hydrogen adsorption free energy, ΔG_H, is generally used as a descriptor of HER activity,[41] where for an optimal electrocatalyst, there is an appropriate balance between the strength of hydrogen adsorption (Volmer, Eq 2) and desorption (Heyrovsky/Tafel, Eqs 3 and 4) from the surface. In other words, if the binding energy is too low (*i.e.*, ΔG_H less negative), the adsorption step (Eq 2) will limit the rate of reaction and likewise the desorption step (Eqs 3 and 4), if the binding energy is too high (*i.e.*, ΔG_H more negative). Thus ΔG_H values for the low index planes of iron were calculated using DFT, as presented in Table 2, for the adsorption sites depicted in the Supporting Information, Figure S6. In order to contextualize these values, a classical volcano-type relationship is assumed, taking value calculated for a Pt(111) surface (also presented in Table 2) as the approximate value for the 'peak' of the volcano.[42-43] Note that the ΔG_H values calculated for Pt(111) are consistent with previous DFT studies.[44-45]

Table 2. ΔG_H values calculated for each adsorption site on the (111) plane of Pt and each of the low index planes (100, 101 and 111) of Fe.

Crystal Plane	Adsorption Location	ΔG_H / eV
Pt(111)	Top	-2.75
	HCP (Hollow)	-2.72
	FCC (Hollow)	-2.77
	Bridge	-2.72
Fe(100)	Bridge	-3.00
	Hollow	-2.97
	On Top	-2.44
Fe(101)	On Top	-2.65
	Hollow	-3.32
	Short Bridge	-3.13
	Long Bridge	-3.28
Fe(111)	On Top	-2.50
	Hollow	-2.30

The calculated ΔG_H values in Table 2 are broadly consistent with previous DFT studies on Fe,[46-47] as well as experimentally calculated Fe-H binding energies.[48] Using the example of the (100) plane, the ΔG_H values for different adsorption sites are more (*e.g.*, Bridge) and less (*e.g.*, On Top) negative than the volcano "peak" [*i.e.*, Pt(111)], meaning the different sites will fall on the ascending and descending branches of the volcano plot,[42-43] respectively, likewise for different grains [*e.g.*, compare Fe(101) and Fe(111)]. This suggests that the rate determining step for HER (equations 2 – 4, above) may vary between adsorption site on a given low index plane, as well as between different low index planes. In any case, taking Pt(111) as the ideal case, we can assume that sites with ΔG_H values closest to Pt(111) will be more facilitative of the HER. Thus, we take the difference between the average ΔG_H

value (from all adsorption sites) for Pt(111), $\Delta G_{\mathrm{H}}^{\mathrm{Pt(111)}}$, and the average ΔG_{H} value for each low index plane, $\Delta G_{\mathrm{H}}^{\mathrm{Fe(hkl)}}$ on Fe as a qualitative indicator of relative HER kinetics, as summarized in Table 3.

Table 3. The calculated average ΔG_{H} deviations for each of the adsorption sites on the low index orientations of Fe from the average ΔG_{H} value calculated for Pt(111).

Crystal Plane	$\boldsymbol{\left\lvert \Delta G_{\mathrm{H}}^{\mathrm{Fe(hkl)}} - \Delta G_{\mathrm{H}}^{\mathrm{Pt(111)}} \right\rvert}$ **/ eV**
Fe(100)	0.26
Fe(101)	0.40
Fe(111)	0.34

The $\left|\Delta G_{\mathrm{H}}^{\mathrm{Fe(hkl)}} - \Delta G_{\mathrm{H}}^{\mathrm{Pt(111)}}\right|$ values increase in the order (100) < (111) < (101), which agrees with the experimentally measured i_{surf} values measured on low carbon steel (Figure 3). Despite the agreement, this comparison should be taken *cum grano salis* due to the number of assumptions/simplifications made. First, the DFT model assumes a pristine crystal lattice of Fe (*i.e.*, no imperfections), whereas for a real low carbon steel surface there are likely to be multiple types of crystallographic defects,[49] some of which are considered below (*e.g.*, grain boundaries). Second, the solvent and anions have not been explicitly considered in the DFT simulations, the latter of which is known to influence HER kinetics on Fe surfaces (*e.g.*, HER inhibition by Cl^- adsorption).[50] Third, although the average $\left|\Delta G_{\mathrm{H}}^{\mathrm{Fe(hkl)}} - \Delta G_{\mathrm{H}}^{\mathrm{Pt(111)}}\right|$ values (Table 3) do follow the experimental trend in i_{surf} (Figure 3), the calculated ΔG_{H} values (Table 2) are site-specific, meaning each low-index orientation possesses a range of sites with differing HER activities.

Thus, an important outcome from these findings is that while the classical volcano relationship is a convenient and powerful way for predicting the macroscale activity of different materials, as in HER electrocatalysis,[20] it is perhaps oversimplified when predicting the local (nanoscale) response of a heterogeneous electrode surface (*e.g.*, polycrystalline metal). For example, the data in Table 2 suggest that the different low-index planes, or indeed the different adsorption sites within a given low-index plane of BCC iron may have large (order-of-magnitude) differences in HER activity, whereas the experimentally determined HER rates were found to show only a subtle grain dependence (Figures 2 and 3). In reality, as we show below, the rate of HER (and the susceptibility to corrosion-related phenomena) across a (non-ideal) polycrystalline alloy surface is more likely to be influenced by crystallographic defects, *e.g.*, grain boundaries and inclusions.

HER activity at grain boundaries. We next consider the HER activity at grain boundaries between crystallites on polycrystalline surfaces, for which SECCM is becoming a particularly powerful technique.[17, 33] The grain boundaries of polycrystalline metals are critically important in the context of corrosion, serving as sites for well-documented phenomena such as intergranular corrosion.[51] The intergranular corrosion of steels is commonly attributed to metallurgical features such as the enrichment of detrimental impurities or the depletion of beneficial alloying elements at grain boundaries.[52] This change in surface chemistry often results in preferential dissolution or in some cases, an enhancement in the cathodic half-cell process(es) at grain boundaries.[51]

EBSD and corresponding spatially-resolved i_{surf} maps of a grain boundary (with misorientation angles marked) that exhibits enhanced HER activity are shown Figure 4a and b, respectively. Evidently, elevated cathodic currents are detected at the grain boundary termination (*ca.* 50% increase compared to the surrounding grains), are clear from Figure 4b. It should be noted that the difference in HER currents between different low-index grains is on the order of 5−20% (see Figure 3), demonstrating that crystallographic defects such as grain boundaries are likely to be far more influential on cathodic corrosion-processes compared to variations in crystal orientation. A time-resolved video of the i_{surf} response at this grain boundary can also be found in the Supporting Information, Movie S2. A further two examples are also presented in Figure 4c and d. It is interesting to note that not all of the grain boundaries exhibit enhanced HER activity (*vide infra*), clear from the i_{surf} maps in Figure 4, as well as Figure 2, above. It should also be noted that in all cases, the elevated currents at the grain boundaries cannot be attributed to distortion of the SECCM meniscus cell (*i.e.*, changes in the probed surface area), as the topographical variation between neighboring grains is on the sub-10 nm scale, confirmed through the synchronously obtained *z*-height data, plotted in the Supporting Information, Figure S7. Additionally, the Supporting Information, Figure S5, shows that there is no variation in the wetting between scanning points located at positions on and adjacent to grain boundaries.

Several factors may result in enhanced catalytic activity at grain boundaries. Surface defects, such as grain boundaries, comprise coordinatively unsaturated sites (*i.e.*, atoms with low lattice

coordinate numbers) that can serve as the "active sites" for electrocatalytic processes.[3, 53] Indeed, such an effect was proposed in a recent SECCM study,[17] where enhanced electrochemical CO_2 reduction activity was identified at grain boundaries on polycrystalline Au. Another possibility is that changes in the surface chemistry at grain boundaries (*i.e.*, impurity enrichment or depletion) may give rise to a catalytically active surface that can facilitate the HER. Although we cannot distinguish between these possibilities herein, the results in Figure 4 demonstrate unequivocally that certain grain boundaries would be more likely to serve as cathodic sites on a macroscopic surface, during atmospheric corrosion (*i.e.*, in the presence of acid rain).

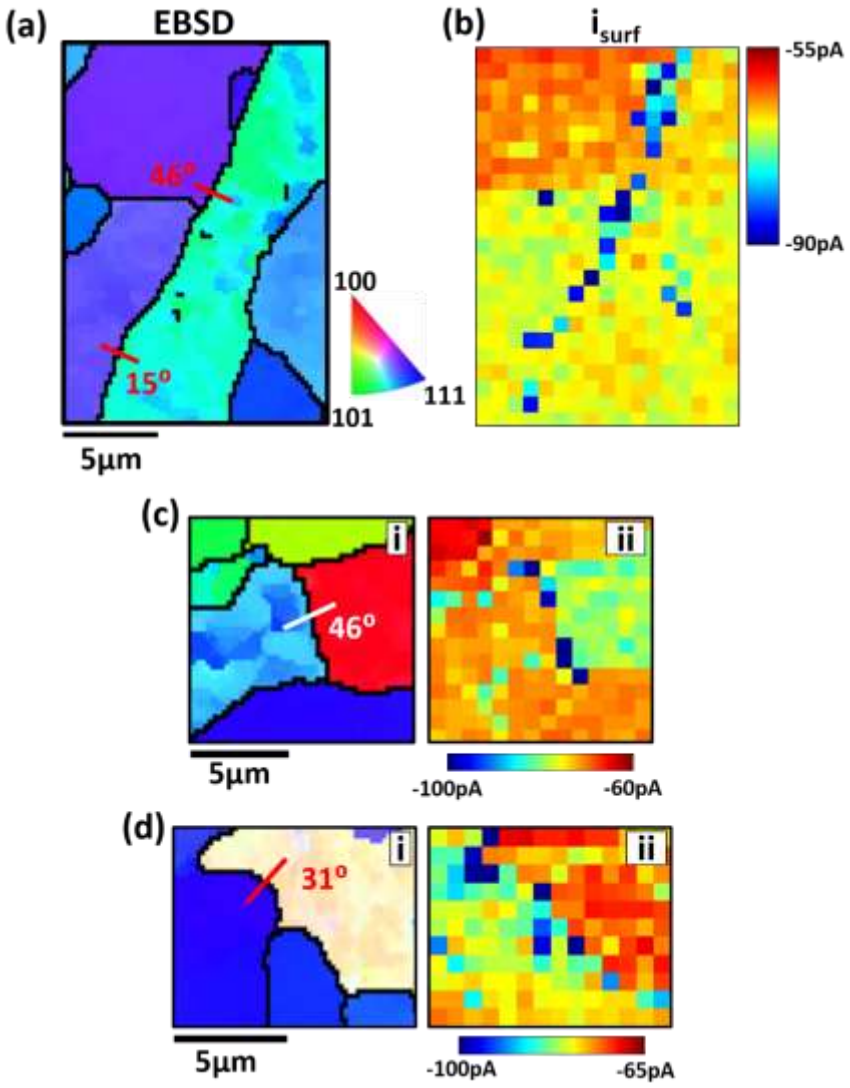

Figure 4. (a) EBSD map of a "cathodically active" grain boundary, with the misorientation between the two neighboring grains labelled inset. **(b)** Spatially-resolved i_{surf} map of the average response from 7.2 to 9.8 ms during a −1.337 V vs Ag/AgCl reduction pulse, in the area of the surface shown in (a). **(c)** and **(d)** EBSD-SECCM i_{surf} map comparisons for two more examples of grain boundaries with enhanced HER activity. There is no interpolation of data in the SECCM images.

HER activity at manganese sulfide inclusions. We now consider the response of individual sub-micron MnS inclusions. Figure 5a shows an SEM image of an area scanned using SECCM, with the corresponding spatially-resolved i_{surf} map shown in Figure 5b. The dark "spots" in Figure 5a, two of which are highlighted by the white box, are MnS inclusions, confirmed by performing EDS; sulfur map and spectra shown in Figure 5c and d, respectively. Focusing on the electrochemical map in Figure 5b, there are two blue pixels indicating off-scale current magnitudes corresponding to the sub-micron MnS inclusions, confirming these sites as local HER "hot spots". Similarly to the case for grain boundaries, the catalytic HER current measured at individual inclusions (up to *ca.* 100% compared to the surrounding grains) is far more significant compared to the difference in activity observed between grains of different crystal orientation (Figure 3). Indeed, the exceptionally high activity of these sites is clear to see from the electrochemical activity maps in Figures 2 and 5, which is further supported by the detection of a range of other inclusions, as shown in the Supporting Information, Figure S8.

The EDC technique has previously been used to study the local dissolution of large MnS inclusions in steel[54-55] and we have also used SECCM to observe similar behavior on low carbon steel, in neutral pH media.[4] Here, we have been able to measure the electrochemical (electrocatalytic) activity of inclusions (*ca.* 0.2 – 1 μm in size) more directly (*i.e.*, the inclusions constitute all or most of the probed area). Large MnS inclusions have previously been shown to be responsible for enhanced hydrogen trapping on steel surfaces, which can lead to hydrogen induced cracking,[56-57] and blistering at

these sites.[58] Our results further emphasize the importance of inclusions as highly active cathodic sites on polycrystalline low carbon steel.

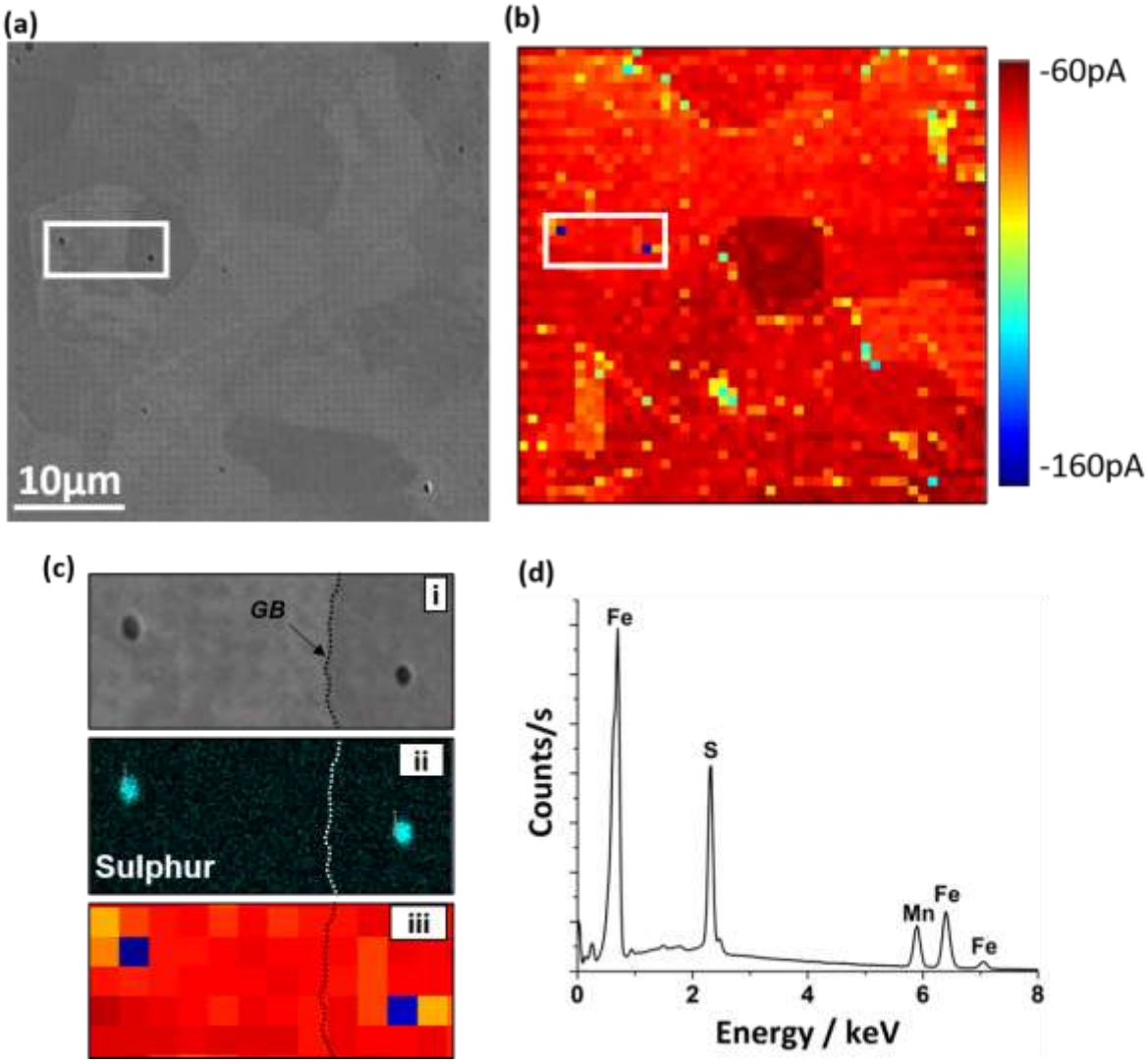

Figure 5. (a) SEM image of the area of low carbon steel scanned with SECCM. The matrix of 50 × 50 scanning points (pixels) can be seen as dark spots on the surface. The darker spots, two of which are highlighted, are MnS inclusions. **(b)** Corresponding spatially resolved i_{surf} map (E_{app} = −1.337 V vs Ag/AgCl), with no interpolation of data. **(c)** Zoomed-in (i) SEM (ii) EDS sulfur map and (iii) i_{surf} images of the boxed area highlighted in (a) and (b). **(d)** EDS spectra of the left inclusion shown in (c). Note that the i_{surf} values are the average of the last six data points (*i.e.*, 7.2 to 9.8 ms).

Conclusions

In this study, we have leveraged recent technical advances in scanning electrochemical cell microscopy (SECCM) to investigate the structure-dependent cathodic activity of low carbon steel in aqueous sulfuric acid (pH ≈ 2.3), in the context of atmospheric (acid rain) corrosion. Focusing on the HER, and using a fine nanopipet probe (diameter ≈ 150 nm) in a fast chronoamperometric (*i*–*t*) scan-hopping protocol (*ca.* 1 s pixel^{-1}), we have shown unequivocally that the rate of this reaction varies spatially across the surface of low carbon steel. By combining these spatially-resolved electrochemical data with co-located structural information from SEM, EBSD and EDS in a correlative electrochemical multi-microscopy approach, HER activity on the low-index planes was shown to increase slightly in the order of (100) > (111) > (101), which we attempted to explain through the calculation of grain-dependent ΔG_H values. The high spatial-resolution of SECCM also allowed grain boundary terminations and (sub-micron) MnS inclusions to be directly interrogated; these surface defects exhibit greatly enhanced HER activity compared to the crystallographic planes, indicting them as likely "cathodic sites" during macroscopic (*e.g.*, atmospheric) corrosion. Overall, this study further demonstrates the great potential of SECCM in corrosion science and electrocatalysis. A holistic view of structure-activity of (electro)materials results when local electrochemical maps and movies are combined with co-located microscopy/spectroscopy, and experiments are further supported by theory (*e.g.*, DFT calculations).

Associated Content

Supporting Information.

Approach curve (Figure S1); linear-sweep voltammograms in the presence and absence of air (Figure S2); i_{surf}–t transient during landing at a passive potential (Figure S3); typical Q–t curve and calculation of passive film charge (Figure S4); SEM image of SECCM droplet cell footprints (Figure S5); adsorption sites on low-index planes of iron (Figure S6); corresponding topographical maps obtained synchronously during SECCM (Figure S7) and; further examples of active MnS inclusions, detected using SECCM (Figure S8).

Time resolved movie of surface current at low carbon steel during reduction pulse (Movie S1) and; time resolved movie of surface current measured at grain boundary of low carbon steel during reduction pulse (Movie S2).

Acknowledgements

This work was supported by an iCASE award to LY from the EPSRC and Tata Steel Research and Development. VS acknowledges financial support from the European Union's Horizon 2020 research and innovation programme under grant agreement 792948 (NELMA). CLB acknowledges financial support from the Ramsay Memorial Fellowship Trust. PRU gratefully acknowledges support from a Royal Society Wolfson Research Merit Award. The authors also thank Dr Digvijay Thakur from Tata Steel Research and Development for helpful discussions.

References

1. Suwas, S.; Ray, R. K., *Crystallographic Texture of Materials*; Springer-Verlag: London, 2014.
2. McCafferty, E., *Introduction to Corrosion Science*; Springer: London, 2010.
3. Bentley, C. L.; Kang, M.; Unwin, P. R., Nanoscale Surface Structure-Activity in Electrochemistry and Electrocatalysis. *J. Am. Chem. Soc.* **2019**, *141*, 2179-2193.
4. Yule, L. C.; Bentley, C. L.; West, G.; Shollock, B. A.; Unwin, P. R., Scanning electrochemical cell microscopy: A versatile method for highly localised corrosion related measurements on metal surfaces. *Electrochim. Acta* **2019**, *298*, 80-88.
5. Ebejer, N.; Güell, A. G.; Lai, S. C. S.; McKelvey, K.; Snowden, M. E.; Unwin, P. R., Scanning electrochemical cell microscopy: a versatile technique for nanoscale electrochemistry and functional imaging. *Annu. Rev. Anal. Chem.* **2013**, *6*, 329-51.
6. Bentley, C. L.; Kang, M.; Unwin, P. R., Scanning electrochemical cell microscopy: New perspectives on electrode processes in action. *Curr. Opin. Electrochem.* **2017**, *6*, 23-30.
7. Böhni, H.; Suter, T.; Schreyer, A., Micro- and nanotechniques to study localized corrosion. *Electrochim. Acta* **1995**, *40*, 1361-1368.
8. Bard, A. J.; Fan, F. R. F.; Kwak, J.; Lev, O., Scanning electrochemical microscopy. Introduction and principles. *Anal. Chem.* **1989**, *61*, 132-138.
9. Payne, N. A.; Stephens, L.; Mauzeroll, J., The Application of Scanning Electrochemical Microscopy to Corrosion Research. *Corrosion* **2017**, *73*, 759-780.
10. Bentley, C. L.; Kang, M.; Unwin, P. R., Nanoscale Structure Dynamics within Electrocatalytic Materials. *J. Amer. Chem. Soc.* **2017**, *139*, 16813-16821.
11. Bentley, C. L.; Unwin, P. R., Nanoscale electrochemical movies and synchronous topographical mapping of electrocatalytic materials. *Faraday Discuss.* **2018**, *210*, 365-379.
12. Tao, B.; Yule, L. C.; Daviddi, E.; Bentley, C. L.; Unwin, P. R., Correlative electrochemistry-microscopy of Li-ion (de)intercalation at series of individual $LiMn_2O_4$ particles. *Angew. Chem.-Int. Edit.* **2019**, *58*, 4606-4611.
13. Bentley, C. L.; Kang, M.; Maddar, F.; Li, F.; Walker, M.; Zhang, J.; Unwin, P. R., Electrochemical Maps and Movies of the Hydrogen Evolution Reaction on Natural Crystals of Molybdenite (MoS 2): Basal vs. Edge Plane Activity. *Chem. Sci.* **2017**, *8*, 6583-6593.
14. Hill, J. W.; Hill, C. M., Directly Mapping Photoelectrochemical Behavior within Individual Transition Metal Dichalcogenide Nanosheets. *Nano Lett.* **2019**, *19*, 5710-5716.
15. Chen, C.-H.; Meadows, K. E.; Cuharuc, A.; Lai, S. C. S.; Unwin, P. R., High Resolution Mapping of Oxygen Reduction Reaction Kinetics at Polycrystalline Platinum Electrodes. *Phys. Chem. Chem. Phys.* **2014**, *16*, 18545-18552.

16. Wang, Y.; Gordon, E.; Ren, H., Mapping the Nucleation of H2 Bubbles on Polycrystalline Pt via Scanning Electrochemical Cell Microscopy. *J. Phys. Chem. Lett.* **2019**, *10*, 3887-3892.

17. Mariano, R. G.; McKelvey, K.; White, H. S.; Kanan, M. W., Selective increase in CO2electroreduction activity at grain-boundary surface terminations. *Science* **2017**, *358*, 1187-1192.

18. Unwin, P. R.; Güell, A. G.; Zhang, G., Nanoscale Electrochemistry of sp^2 Carbon Materials: From Graphite and Graphene to Carbon Nanotubes. *Acc. Chem. Res.* **2016**, *49*, 2041-2048.

19. Andreatta, F.; Fedrizzi, L., The use of the electrochemical micro-cell for the investigation of corrosion phenomena. *Electrochim. Acta* **2016**, *203*, 337-349.

20. Seh, Z. W.; Kibsgaard, J.; Dickens, C. F.; Chorkendorff, I.; Norskov, J. K.; Jaramillo, T. F., Combining theory and experiment in electrocatalysis: Insights into materials design. *Science* **2017**, *355*.

21. Pound, B., Chapter 2.2 Hydrogen Ingress during Corrosion In *Corrosion and Oxide Films*, Stratmann, M.; Frankel, G., Eds. Wiley-VCH: Germany, 2003; Vol. 4, pp 108-155.

22. Fontana, M. G., *Corrosion Engineering*, 3rd ed.; McGraw-Hill, 1986.

23. Kohn, W.; Sham, L. J., Self-Consistent Equations Including Exchange and Correlation Effects. *Physical Review* **1965**, *140*, A1133-A1138.

24. Monkhorst, H. J.; Pack, J. D., Special points for Brillouin-zone integrations. *Phys. Rev. B* **1976**, *13*, 5188-5192.

25. Vanderbilt, D., Soft self-consistent pseudopotentials in a generalized eigenvalue formalism. *Phys. Rev. B* **1990**, *41*, 7892-7895.

26. Dal Corso, A., Pseudopotentials periodic table: From H to Pu. *Comput. Mater. Sci.* **2014**, *95*, 337-350.

27. Giannozzi, P.; Baroni, S.; Bonini, N.; Calandra, M.; Car, R.; Cavazzoni, C.; Ceresoli, D.; Chiarotti, G. L.; Cococcioni, M.; Dabo, I., et al., QUANTUM ESPRESSO: a modular and open-source software project for quantum simulations of materials. *J. Phys. Condens. Matter* **2009**, *21*, 395502.

28. Neugebauer, J.; Scheffler, M., Adsorbate-substrate and adsorbate-adsorbate interactions of Na and K adlayers on Al(111). *Phys. Rev. B* **1992**, *46*, 16067-16080.

29. Pulay, P., Convergence acceleration of iterative sequences. the case of scf iteration. *Chem. Phys. Lett.* **1980**, *73*, 393-398.

30. Pfrommer, B.; Cote, M.; Louie, S. G.; Cohen, M. L., Relaxation of Crystals with the Quasi-Newton Method. *J. Comput. Phys.* **1997**, *131*, 233-240.

31. Tsuru, T.; Tamiya, K. I.; Nishikata, A., Formation and growth of micro-droplets during the initial stage of atmospheric corrosion. *Electrochim. Acta* **2004**, *49*, 2709-2715.

32. Davenport, A. J.; Oblonsky, L. J.; Ryan, M. P.; Toney, M. F., The Structure of the Passive Film That Forms on Iron in Aqueous Environments. *J. Electrochem. Soc.* **2000**, *147*, 2162-2173.

33. Aaronson, B. D. B.; Chen, C. H.; Li, H. J.; Koper, M. T. M.; Lai, S. C. S.; Unwin, P. R., Pseudo-Single-Crystal Electrochemistry on Polycrystalline Electrodes: Visualizing Activity at Grains and Grain Boundaries on Platinum for the Fe^{2+}/Fe^{3+} Redox Reaction. *J. Am. Chem. Soc.* **2013**, *135*, 3873-3880.

34. Longsworth, L. G., Temperature Dependence of Diffusion in Aqueous Solutions. *J. Phys. Chem.* **1954**, *58*, 770-773.

35. Momotenko, D.; Byers, J. C.; McKelvey, K.; Kang, M.; Unwin, P. R., High-Speed Electrochemical Imaging. *ACS Nano* **2015**, *9*, 8942-8952.

36. Eftekhari, A., Electrocatalysts for hydrogen evolution reaction. *Int. J. Hydrog. Energy* **2017**, *42*, 11053-11077.

37. Markovic, N. M.; Sarraf, S. T.; Gasteiger, H. A.; Ross Jr, P. N., Hydrogen electrochemistry on platinum low-index single-crystal surfaces in alkaline solution. *Faraday Trans.* **1996**, *92*, 3719-3725.

38. Hoshi, N.; Asaumi, Y.; Nakamura, M.; Mikita, K.; Kajiwara, R., Sructural Effects on the Hydrogen Oxidation Reaction on n(111)-(111) Surface of Platinum. *J. Phys. Chem. C* **2009**, *113*, 16843-16846.

39. Dadfarnia, M.; Nagao, A.; Wang, S.; Martin, M. L.; Somerday, B. P.; Sofronis, P., Recent advances on hydrogen embrittlement of structural materials. *Int. J. Fract.* **2015**, *196*, 223-243.

40. Snowden, M. E.; Güell, A. G.; Lai, S. C. S.; McKelvey, K.; Ebejer, N.; O'Connell, M. A.; Colburn, A. W.; Unwin, P. R., Scanning Electrochemical Cell Microscopy: Theory and Experiment for Quantitative High Resolution Spatially-Resolved Voltammetry and Simultaneous Ion-Conductance Measurements. *Anal. Chem.* **2012**, *84*, 2483-2491.

41. Norskov, J. K.; Bligaard, T.; Logadottir, A.; Kitchin, J. R.; Chen, J. G.; Pandelov, S.; Stimming, U., Trends in the Exchange Current for Hydrogen Evolution. *J. Electrochem. Soc.* **2005**, *152*, J23-J26.

42. Santos, E.; Quaino, P.; Schmickler, W., Theory of electrocatalysis: hydrogen evolution and more. *Phys. Chem. Chem. Phys.* **2012**, *14*, 11224-11233.

43. Strmcnik, D.; Lopes, P. P.; Genorio, B.; Stamenkovic, V. R.; Markovic, N. M., Design principles for hydrogen evolution reaction catalyst materials. *Nano Energy* **2016**, *29*, 29-36.

44. Kozlov, S. M.; Aleksandrov, H. A.; Neyman, K. M., Adsorbed and Subsurface Absorbed Hydrogen Atoms on Bare and MgO(100)-Supported Pd and Pt Nanoparticles. *J. Phys. Chem. C* **2014**, *118*, 15242-15250.

45. Yan, L.; Sun, Y.; Yamamoto, Y.; Kasamatsu, S.; Hamada, I.; Sugino, O., Hydrogen adsorption on Pt(111) revisited from random phase approximation. *J. Chem. Phys.* **2018**, *149*, 164702.

46. Ferrin, P.; Kandoi, S.; Nilekar, A. U.; Mavrikakis, M., Hydrogen adsorption, absorption and diffusion on and in transition metal surfaces: A DFT study. *Surf. Sci.* **2012**, *606*, 679-689.

47. Wang, T.; Wang, S.; Luo, Q.; Li, Y.-W.; Wang, J.; Beller, M.; Jiao, H., Hydrogen Adsorption Structures and Energetics on Iron Surfaces at High Coverage. *J. Phys. Chem. C* **2014**, *118*, 4181-4188.

48. Bozso, F.; Ertl, G.; Grunze, M.; Weiss, M., Chemisorption of hydrogen on iron surfaces. *Appl. Surf. Sci.* **1977**, *1*, 103-119.

49. Reed-Hill, R. E., *Physical Metallurgy Principles*; PWS: U.S.A, 1994.

50. Vracar, L. J.; Drazic, D. M., Influence of chloride adsorption on hydrogen evolution reaction on iron. *J. Electroanal. Chem.* **1992**, *339*, 269-279.

51. Scully, J. R., Chaper 4.3 Intergranular Corrosion. In *Corrosion and Oxide Films*, Frankel, G.; Stratmann, M., Eds. Wiley-VCH: Germany, 2003; Vol. 4, pp 344-380.

52. Briant, C. L.; Andresen, P. L., Grain Boundary Segregation in Austenitic Stainless Steels and its Effect on Intergranular Corrosion and Stress Corrosion Cracking. *Metall. Mater. Trans. A* **1987**, *19*, 495-504.

53. O'Mullane, A. P., From single crystal surfaces to single atoms: investigating active sites in electrocatalysis. *Nanoscale* **2014**, *6*, 4012-4026.

54. Suter, T.; Bohni, H., Microelctrodes for corrosion studies in microsystems. *Electrochim. Acta* **2001**, *47*, 191-199.

55. Webb, E. G.; Suter, T.; Alkire, R. C., Microelectrochemical measurements of the dissolution of single MnS inclusions, and the prediction of the critical conditions for pit initiation on stainless steel. *J. Electrochem. Soc.* **2001**, *148*, B186-B195.

56. Peng, Z.; Liu, J.; Huang, F.; Hu, Q.; Cheng, Z.; Liu, S.; Cheng, Y., Effect of Submicron-Scale MnS Inclusions on Hydrogen Trapping and HIC Susceptibility of X70 Pipeline Steels. *Steel Res. Int.* **2018**, *89*, .

57. Muto, I.; Shinozaki, J.; Omura, T.; Numata, M.; Hara, N., Microelectrochemical Investigation of Hydrogen Absorption and Dissolution Behaviour of MnS inclusions in Carbon Steel. *ECS Trans.* **2011**, *33*, 9-20.

58. Ren, X.; Chu, W.; Li, J.; Su, Y.; Qiao, L., The effects of inclusions and second phase particles on hydrogen-induced blistering in iron. *Mater. Chem. Phys.* **2008**, *107*, 231-235.

TOC Graphic:

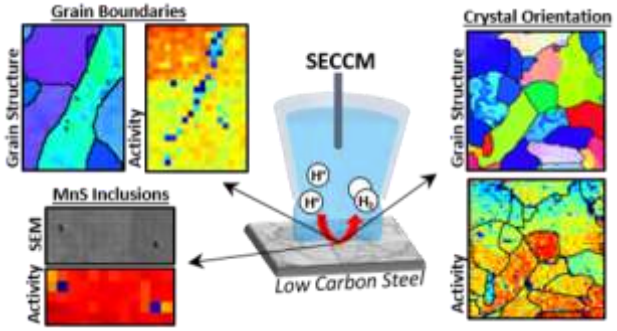
Grain Boundaries
Grain Structure
Activity
SECCM
Crystal Orientation
Grain Structure
Activity
MnS Inclusions
SEM
Activity
Low Carbon Steel